The aerodynamics of hovering flight in *Drosophila*

Steven N. Fry[1],*, Rosalyn Sayaman[2] and Michael H. Dickinson[2]

[1]*Institute of Neuroinformatics, University/ETH Zürich, Switzerland* and [2]*California Institute of Technology, Mail Code 138-78, Pasadena, CA 91125, USA*

*Author for correspondence (e-mail: steven@ini.phys.ethz.ch)

Summary

Using 3D infrared high-speed video, we captured the continuous wing and body kinematics of free-flying fruit flies, *Drosophila melanogaster*, during hovering and slow forward flight. We then 'replayed' the wing kinematics on a dynamically scaled robotic model to measure the aerodynamic forces produced by the wings. Hovering animals generate a U-shaped wing trajectory, in which large drag forces during a downward plunge at the start of each stroke create peak vertical forces. Quasi-steady mechanisms could account for nearly all of the mean measured force required to hover, although temporal discrepancies between instantaneous measured forces and model predictions indicate that unsteady mechanisms also play a significant role. We analyzed the requirements for hovering from an analysis of the time history of forces and moments in all six degrees of freedom. The wing kinematics necessary to generate sufficient lift are highly constrained by the requirement to balance thrust and pitch torque over the stroke cycle. We also compare the wing motion and aerodynamic forces of free and tethered flies. Tethering causes a strong distortion of the stroke pattern that results in a reduction of translational forces and a prominent nose-down pitch moment. The stereotyped distortion under tethered conditions is most likely due to a disruption of sensory feedback. Finally, we calculated flight power based directly on the measurements of wing motion and aerodynamic forces, which yielded a higher estimate of muscle power during free hovering flight than prior estimates based on time-averaged parameters. This discrepancy is mostly due to a two- to threefold underestimate of the mean profile drag coefficient in prior studies. We also compared our values with the predictions of the same time-averaged models using more accurate kinematic and aerodynamic input parameters based on our high-speed videography measurements. In this case, the time-averaged models tended to overestimate flight costs.

Key words: fruit fly, *Drosophila melanogaster*, flight, aerodynamics, power, biomechanics, behavior.

Introduction

The apparent ease with which fruit flies and many other small insects hover obscures the challenge of this ostensibly simple task. In order to hover, the flapping wings must generate sufficient lift to offset body weight while simultaneously maintaining a precise balance of aerodynamic forces and moments to stabilize the body. The requisite wing motion is driven by indirect flight muscles, which provide elevated mechanical power, and direct control muscles, which subtly adjust wing motion on a cycle-by-cycle basis. Hovering has been the focus of many prior aerodynamic studies of insect flight because the power requirements are extreme, but the aerodynamic complications caused by forward movement of the body are absent (tethered flying: Weis-Fogh, 1972; Ellington, 1984a; free flying: Willmott and Ellington, 1997). Due to the difficulties related with precisely measuring the kinematics and the resulting aerodynamic forces of flapping wings, much prior work has relied on time-averaged measures of flight performance (Dudley, 2000). This approach has the benefit of providing a theoretical framework that can be applied, in principle, without detailed knowledge about the time course of wing kinematics and forces. However, these models incorporate several critical assumptions and use a number of kinematic and aerodynamic parameters that may be difficult to estimate reliably. Furthermore, time-averaged approaches are not sufficient to address questions relating to flight control (Dudley, 2000; Taylor, 2001).

Although many prior studies have succeeded in capturing wing kinematics in free flight using high speed cine or video (Wakeling and Ellington, 1997; Willmott and Ellington, 1997), such methods do not provide a measure of instantaneous aerodynamic forces. One means of circumventing this limitation is to employ computational fluid dynamic (CFD) simulations to estimate forces from known kinematics (e.g. Sun and Wu, 2003; Wu and Sun, 2004; Sun and Lan, 2004). These methods show great promise as computation power increases and algorithms improve, although concerns still remain regarding the accuracy of simulating unsteady 3D flows. Another, complimentary, approach is to measure the

instantaneous forces by 'replaying' free-flight kinematics on a dynamically scaled physical model equipped with suitable force sensors (Fry et al., 2003 and supporting on-line material at http://www.sciencemag.org/cgi/data/300/5618/495/DC1/1). Although there are limitations to the accuracy with which the morphology and motion of an insect wing can be replicated by the robot, this method does permit a time-resolved estimate of aerodynamics, and therefore an analysis of energetics and control. Furthermore, experiments with physical models are essential for testing the accuracy of CFD simulations.

Another common approach in the study of insect flight is the use of tethered preparations for the measurement of wing kinematics, flight forces (Cloupeau et al., 1979; Buckholz, 1981; Zanker, 1990a,b; Dickinson and Götz, 1996) and energetic costs (Lehmann and Dickinson, 1997). The downside of this approach is that tethering may alter the mechanical properties of the thorax or influence an insect's behavior due to unnatural sensory stimulation. Although the recent generation of tethered flight simulators can provide detailed visual stimuli, most cannot provide mechanosensory feedback (but see Sherman and Dickinson, 2003). Realistic sensory conditions are especially important for studies of flight control, because sensory feedback from eyes, ocelli and (in flies) halteres provides essential reafferent feedback from body motion (Nalbach, 1993; Nalbach and Hengstenberg, 1994; Dickinson, 1999; Sherman and Dickinson, 2003).

In this study we present detailed measurements of the continuous time course of 3D wing motion and flight forces measured in free flying and tethered fruit flies *Drosophila melanogaster*. We examine the aerodynamic mechanisms underlying hovering flight by comparing the measured time course of aerodynamic forces with those predicted from a quasi steady-state model. Next, we examine flight control by analyzing the time course of aerodynamic forces and torques in all six degrees of freedom (d.f.). We also assess the effects of tethering on flight performance by comparing wing kinematics, forces and moments generated under free and tethered conditions. Finally, we compare power requirements derived from measured instantaneous kinematics and forces with estimates based on time-averaged models. In sum, the results provide a detailed view of the aerodynamics, control and energetics of hovering flight in *Drosophila*.

Materials and methods
3D high-speed videography

The methods developed to acquire continuous measurements of instantaneous wing and body kinematics, as well as aerodynamic forces, have been described previously in an abbreviated form (Fry et al., 2003 and supporting online material at http://www.sciencemag.org/cgi/data/300/5618/495/DC1/1). Here, we give a more complete description of the methods applied to free and tethered flying flies. We filmed the free-flight behavior of fruit flies *Drosophila melanogaster* Meigen in an enclosed flight chamber built from translucent white acetate (Fig. 1A). Three orthogonally aligned high-speed cameras

(Kodak MotionCorder, 5000 frames s^{-1}, shutter speed 50 μs, resolution 146×88 pixels), located outside the cube, were aimed at a small central region through circular windows in the side walls. We backlit each camera view using densely packed arrays of near infrared (λ=880 nm) light emitting diodes (LED), covered with diffusive tracing paper. The visual system of flies is insensitive in this range of the spectrum (Stark and Johnson, 1980) and consequently the visually mediated components of their flight behavior are not compromised by the elevated light levels required for high-speed filming. Hungry flies have been shown to approach dark objects when attractive odors are present (Frye et al., 2003). We made use of this behavior by starving the flies for at least 5 h prior to each experiment and placing a small black vertical cylinder laced with a drop of vinegar just outside the field of view of the cameras. We then released a large number of flies at a time and manually triggered the cameras when a fly approached the cylinder in view of the cameras. Data collection was limited primarily by the requirement that the fly move through the approximately 0.5 cm^3 cubic zone representing the intersecting fields of view of the three cameras. Flights containing slow straight flight segments interrupted by rapid saccadic turns were selected and downloaded onto the computer's hard disk for later analysis. From six flight sequences of different flies we used 11 straight flight segments for the analysis, comprising a total of 67 stroke cycles, sampled by 1539 frames (approximately 23 frames per stroke cycle, depending on the animal's wing beat frequency). An analysis of the saccadic turns is described elsewhere (Fry et al., 2003). Because fruit flies rarely hovered perfectly in place in our experiments, we included sequences of slow straight flight in the analysis. The advance ratios (forward velocity/wing tip velocity; eq. 23 in Ellington, 1984c) of flights used in the analysis were 0.14 or less (0.073±0.035, mean ± S.D.). Under these conditions, the influence of body velocity on the forces produced by the wings should be quite small. The great similarity of wing kinematics of individuals flying across our chosen range of advance ratios further justifies this assumption.

Measurement of wing and body kinematics

We developed an interactive graphic user interface using Matlab (The MathWorks, Inc.) to extract the 3D body and wing positions from the three images (12 d.f.). The measured positions of the head and tip of the abdomen were adjusted in the display until the best overlap between the measured and displayed body positions was achieved in all three views. Similarly, the position of the wing tip and the wing hinge were measured, after which a wing silhouette was displayed for each wing in each of the three views (Fig. 1B, red and yellow wing silhouette for the right and left wing, respectively). Finally, wing orientation was measured by rotating the model wing spanwise. Typically, several re-adjustments of each parameter were required to obtain a satisfactory match.

We also measured the wing kinematics in tethered flying flies, in combination with an optoelectronic wing beat analyzer (Götz, 1987; Lehmann and Dickinson, 1997) that measured the stroke amplitude and frequency of both wings in real time. Sequences
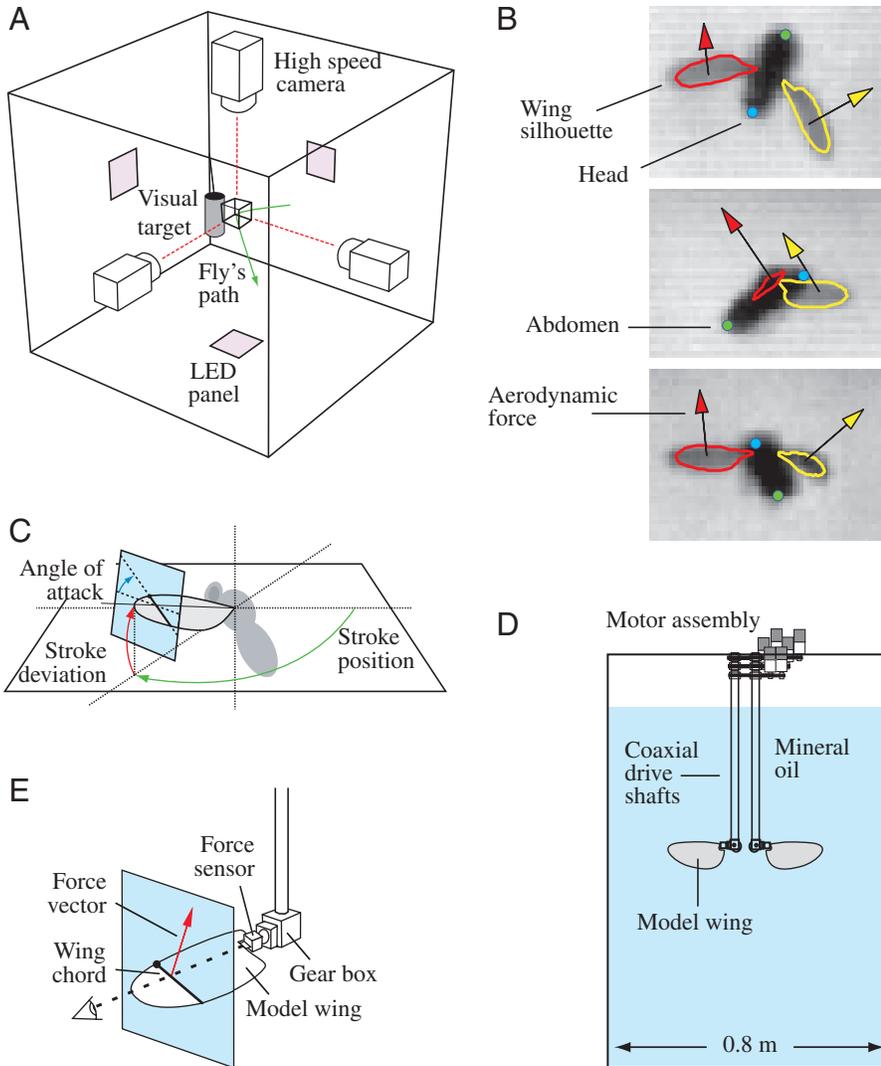
Fig. 1. Measurement of kinematics and forces. (A) 3D high speed videography. Three orthogonally aligned high speed cameras were used to film flies as they entered a small volume (wire-frame) next to a visual target (black cylinder). (B) Examples of frames recorded simultaneously by the three cameras. Body and wing kinematics were measured by matching markers for the head and abdomen, as well as the right (red) and left (yellow) wing in all three images. Arrows show the subsequently measured aerodynamic force projected back onto the images. (C) Wing position in body centered polar coordinates are defined by three angles: Stroke position (0° lateral, downstroke positive), stroke deviation (upward positive) and angle of attack (rotation around wing span, 0° leading edge up, positive rotation brings leading edge forward), following previously used conventions (Sane and Dickinson, 2001). (D) Dynamically scaled robotic wing. Each wing was controlled by three servo motors *via* coaxial drive shafts. Most of our data were acquired using a single-wing configuration. (E) Wing sensor and aerodynamic force. Forces were measured in a plane orthogonal to the wing span. For the analysis, the forces needed to be scaled and transformed into fixed frame coordinates, as shown in B. For further details on the setup refer to Materials and methods. A more detailed description of the robotic wing is given in Dickson and Dickinson (2004).

with roughly similar stroke amplitudes of both wings were used for the analysis to ensure that the fly was not attempting to turn. The methods applied to extract the kinematics were the same as those for free flying flies, whereas the body position remained fixed. For tethered flight, we analyzed a total of 59 stroke cycles (1550 frames) from five different flies.

Measurement of aerodynamic forces

To measure the aerodynamic forces produced by a single wing, its motion in body centered coordinates (Fig. 1C) was played through a newly developed dynamically scaled flapping robot (Fig. 1D,E). The device was similar to one described previously (Dickinson et al., 1999), except that wing motion was controlled by feedback-driven servo-motors and not stepper motors, and the gearing mechanism was improved to lower the effects of backlash (a more detailed description is given in Dickson and Dickinson, 2004; note that our experiments were performed without translation). Inertial forces due to the wing mass of the robot were below the noise limit of our sensor and thus did not contaminate the measurements of aerodynamic force. It seemed justified to

perform the measurements in absence of a second wing, because in none of the sequences we analyzed did the animals exhibit a clap-and-fling behavior (Weis-Fogh, 1973). A control measurement using the robot in a two-wing configuration confirmed the absence of detectable wing–wing interactions. Another potential source of error is that the forces produced by a slowly translating fly were measured on a stationary robot. Although adequate for hovering, the motion of the fly through the air must influence the flow and forces on the flapping wings to some degree.

The stroke frequency of the robotic fly was precisely adjusted to match the calculated Reynolds number of the flapping fly wings (Dickinson et al., 1999). The magnitude of aerodynamic forces acting on an actual fly, F_{Fly}, is related to those measured in the robotic model, F_{Robot}, according to the relationship:

$$F_{Fly} = F_{Robot} \times \frac{\rho_{Air}}{\rho_{Oil}} \times$$

$$\left(\frac{n_{Fly}}{n_{Robot}}\right)^2 \times \left(\frac{R_{Fly}}{R_{Robot}}\right)^2 \times \frac{S_{Fly}}{S_{Robot}} \times \frac{\hat{r}_2^2(S)_{Fly}}{\hat{r}_2^2(S)_{Robot}}, \quad (1)$$

where ρ is fluid density, n is stroke frequency, R is wing length, S is wing area, and $\hat{r}_2^2(S)$ is the normalized second moment of wing area (for a definition, see Ellington, 1984b, p. 25). The values of $\hat{r}_2^2(S)_{\text{robot}}$ and $\hat{r}_2^2(S)_{\text{fly}}$ differed slightly (0.39 and 0.35, respectively), due to a small notch at the base of the robotic wing required to accommodate the force sensor. This calculation of the scaling relationship, which is based on the equivalency of mean force coefficients, is considerably more robust than that previously applied (see supporting on line material in Fry et al., 2003), which is susceptible to small errors in the calculation of Reynolds number. Because it was not possible to capture and weigh the individual flies that we filmed, we estimated each fly's wing area and body mass based on previously measured morphometric relationships (M. H. Dickinson, unpublished). The regression equations for wing area (a, in m^2) as function of wing length (l, in m) was: $a = -2.023 \times 10^{-6} + l1.748 \times 10^{-3}$. The regression for body mass (M_b, in kg) was: $M_b = -2.796 \times 10^{-7} + l4.982 \times 10^{-4}$. Both regressions were derived using the Matlab robust fit function to remove the effects of outliers.

Calculation of torques

The aerodynamic forces measured on the robot were in wing-centered coordinates and required transformation into a fixed reference frame (Haslwanter, 1995). The torque acting on the body based on the aerodynamic forces could be calculated after a number of assumptions were made. The fly's body was assumed rigid and the center of mass was assumed to lie in the sagittal plane, half way along the measured long axis of the fly. To calculate the magnitude of moment about the center of mass of the body, we assumed that the center of pressure of the wing was located 70% along the line connecting the base and tip. A similar value has been confirmed by computational fluid dynamics (Ramamurti and Sandberg, 2002), and experimental measures of the distribution of chord-wise circulation along the wing (Birch and Dickinson, 2001; Birch et al., 2004). The following calculations (Eq. 2–5) apply to a single wing. The effect of both wings was obtained by subsequently adding the contributions of the right and left wing. The aerodynamic torque produced by a wing, $\mathbf{T}_{\text{Aero}}$, is a 3D vector originating at the center of mass of the fly, and can be calculated from the vector product of the moment arm $\mathbf{r}$ and the aerodynamic force $\mathbf{F}_{\text{Aero}}$ as:

$$\mathbf{T}_{\text{Aero}} = \mathbf{r} \times \mathbf{F}_{\text{Aero}} , \qquad (2)$$

where $\mathbf{r}$ points to the center of pressure of the wing. $\mathbf{F}_{\text{Aero}}$ is the force vector representing all fluid forces acting on the wing, scaled according to Eq. 1. The torque component aligned with the principal morphological axes of rotation (yaw, pitch, roll, Fig. 3D–F) is calculated from the scalar product of the total torque and a unit vector pointing in the direction of each rotation axis.

Calculation of instantaneous power

To move its wings, the fly must overcome aerodynamic

resistance and the wing's inertia. Aerodynamic power P_{Aero} can be directly calculated as the scalar product of wing velocity and aerodynamic force:

$$P_{\text{Aero}} = -\mathbf{U}_{\text{P}} \cdot \mathbf{F}_{\text{Aero}} , \qquad (3)$$

where $\mathbf{U}_{\text{P}}$ is the velocity of the wing at the center of pressure. Inertial power P_{Acc} is calculated analogously, as:

$$P_{\text{Acc}} = -\mathbf{U}_{\text{M}} \cdot \mathbf{F}_{\text{Acc}} , \qquad (4)$$

where $\mathbf{U}_{\text{M}}$ is the velocity of the wing at the center of mass, assumed to lie on the wing span 70% of the length toward the wing tip, and $\mathbf{F}_{\text{Acc}}$ is the inertial force required to accelerate the wing. The true positions of the center of mass and pressure (see above) may deviate slightly from the assumed values, consequently resulting in a proportional error in the estimated wing forces; however, the error is expected to be small.

According to Newton's second law, $\mathbf{F}_{\text{Acc}}$ can be calculated from the product of wing mass, M_{Wing}, and wing acceleration:

$$\mathbf{F}_{\text{Acc}} = M_{\text{Wing}} \cdot \frac{d\mathbf{U}_{\text{M}}}{dt} , \qquad (5)$$

with M_{Wing} estimated from the wing area as determined from morphometric regression on wing length (see above), and a previously published value for the mean area density of *Drosophila* wings (Lehmann and Dickinson, 1997). Wing velocity and acceleration were calculated as the first and second derivatives of the measured wing position, respectively. To avoid amplification of measurement error when calculating first and second derivatives of wing position, we applied a suitable b-spline algorithm to smooth the data (Craven and Wahba, 1979; W. Dickson, personal communication). It is important to note that our estimate of inertial power does not include a term resulting from added mass, as in Ellington's time-averaged estimates (Ellington, 1984e). Added mass is an aerodynamic force that scales with Reynolds number and is measured directly by our wing sensor. Thus, the power term resulting from added mass force is lumped into the aerodynamic power term defined in Eq. 3.

Consistent with much of the literature, we present the specific power P^*, i.e. power normalized to muscle mass:

$$P^* = \frac{P}{M_{\text{M}}} , \qquad (6)$$

where the mass of flight muscle, M_{M}, is assumed to contribute to 30% of the total body mass (Lehmann and Dickinson, 1997, p. 1135), which was determined from morphometric regression on wing length (see above).

Estimation of instantaneous specific muscle power

The total instantaneous power required to move the wing, P^*_{Mech}, is the sum of instantaneous aerodynamic and inertial power:

$$P^*_{\text{Mech}} = P^*_{\text{Aero}} + P^*_{\text{acc}} . \qquad (7)$$

When the wings decelerate and little aerodynamic force is

generated toward the end of each half stroke, P^*_{Mech} can be negative. This excess kinetic energy could provide a source of power for the next stroke, provided that it is stored as elastic strain energy within the thorax. Thus, the actual power the flight muscles must generate depends on the time course of P^*_{Mech} and the degree of elastic storage. Assuming all the excess kinetic energy of the wings is stored as elastic energy and released without loss at the start of the subsequent half stroke, the lower estimate of mean muscle power, P^*_{Musc}, is:

$$P^*_{\text{Musc}} = P^*_{\text{Mech,low}} = \overline{P^*_{\text{Mech}}} \,. \tag{8}$$

Conversely, an upper estimate of P^*_{M} is obtained by assuming that excess kinetic energy is completely dissipated as heat (but not accruing an additional cost):

$$P^*_{\text{Musc}} = P^*_{\text{Mech,high}} = \overline{|P^*_{\text{Mech}}|} \,. \tag{9}$$

Time-averaged models

One goal of the paper is to compare power estimates derived from instantaneous forces and kinematics with those derived from prior time-averaged models. For this comparison, we use Ellington's influential models of induced, profile and inertial power (Ellington, 1984e; Lehmann and Dickinson, 1997), based on the time-averaged forces and kinematics. In this case, however, we can use kinematic parameters derived directly from our 3D kinematic analysis and compare the results with our more direct estimates of flight power based on instantaneous free-flight kinematics and forces (Eq. 3–7).

Induced power

Specific induced power is estimated according to Rankine–Froude theory (also see Ellington, 1984d,e) from:

$$P^*_{\text{ind}} = \frac{\boldsymbol{g}}{0.3} \sqrt{\frac{\overline{F_{\text{L}}}}{2\rho\Phi R^2}}\, k \,, \tag{10}$$

where $\boldsymbol{g}$ is the gravitational constant, $\overline{F_{\text{L}}}$ is the mean lift force, ρ is air density (1.2 kg m^{-3}), Φ is the stroke amplitude in radians, R is wing length and k is a correction factor that takes into account the unsteadiness of the wake (Ellington, 1984e). The factor 1/0.3 is used to obtain the power per unit mass of *Drosophila* flight muscles (see above). To apply the above equation to the measured free-flight wing kinematics and flight forces, we calculated Φ, R, k and $\overline{F_{\text{L}}}$. However, it should be noted that whereas the Rankine–Froude model assumes planar motion of the wing, our free-flight measurements indicate significant time-variant deviation from the stroke plane. Lift is defined with respect to the motion of the wing relative to the fluid, and hence depends on the induced velocity ω_0, which can be estimated as (eq. 13 in Ellington, 1984d):

$$\omega_0 = \sqrt{\frac{M_{\text{b}}\boldsymbol{g}}{2\rho}}\, A_0 \,, \tag{11}$$

where $A_0 = \Phi R^2$ for a horizontal stroke plane. Knowledge of ω_0 then allows a more accurate estimation of $\overline{F_{\text{L}}}$ (perpendicular to relative wing velocity).

Profile power

Specific profile power was evaluated according to Ellington's model:

$$P^*_{\text{pro}} = \frac{\rho S n^3 \Phi^3 R^3 \hat{r}_3^3(S)\,\overline{|\mathrm{d}\hat{\phi}/\mathrm{d}\hat{t}|^3}}{16 M_{\text{M}}}\, \overline{C_{\text{D,pro}}} \,, \tag{12}$$

where S is the surface of the two wings, n is the stroke frequency, $\hat{r}_3^3(S)$ is the non-dimensional third moment of wing area, $\overline{|\mathrm{d}\hat{\phi}/\mathrm{d}\hat{t}|^3}$ is the mean cube of the absolute value of non-dimensional angular velocity and $\overline{C_{\text{D,pro}}}$ is the mean profile drag coefficient. For $\hat{r}_3^3(S)$ the published value (Lehmann and Dickinson, 1997) of 0.242 was used. All other parameters were calculated from the measured free-flight wing kinematics and forces (Table 1). $\overline{C_{\text{D,pro}}}$ was estimated in two ways. First, from

$$\overline{C_{\text{D,pro}}} = 7 \,/ \sqrt{Re} \,, \tag{13}$$

an approximation offered by Ellington (eq. 27 in Ellington, 1984e) on empirical measurements of drag on flat plates in steady 2D translating flow. The second calculation was based on the measured mean profile drag, $\overline{F_{\text{D}}}$, and kinematic parameters in our free-flight experiments (Lehmann and Dickinson, 1998):

$$\overline{C_{\text{D,pro}}} = \frac{8\overline{F_{\text{D}}}}{\rho\Phi^2 n^2 R^3 \bar{c}\, \overline{(\mathrm{d}\hat{\phi}/\mathrm{d}\hat{t})^2}\, \hat{t}\hat{r}_2^2(S)} \,, \tag{14}$$

where $\bar{c}$ is the mean wing chord and $\hat{t}$ is the proportion of stroke time (from 0 to 1) over which force is generated. In this case we set $\hat{t}=1$, consistent with our free-flight measures. The mean square of non-dimensional wing velocity, $\overline{(\mathrm{d}\hat{\phi}/\mathrm{d}\hat{t})^2}$, was calculated from the measured wing kinematics.

Inertial power

Inertial power can be estimated (Ellington, 1984e) from:

$$P^*_{\text{acc}} = \frac{\rho S n^3 \Phi^2 R^3 (\mathrm{d}\hat{\phi}/\mathrm{d}\hat{t})_{\text{max}}^2}{2 M_{\text{M}}\boldsymbol{g}}\left[\frac{\rho_{\text{W}}}{\rho}\, \hat{h}\hat{r}_2^2(m) + \frac{\pi S \hat{v}\hat{r}_2^2(v)}{8 R^2}\right], \tag{15}$$

where $(\mathrm{d}\hat{\phi}/\mathrm{d}\hat{t})_{\text{max}}^2$ is the square of the maximum non-dimensional wing velocity, $\hat{r}_2^2(m)$ is the non-dimensional second moment of wing mass, $\hat{v}$ is the non-dimensional virtual mass, $\hat{r}_2^2(v)$ is the non-dimensional second moment of wing virtual mass and $\hat{h}$ is the non-dimensional wing thickness (table 1 in Lehmann and Dickinson, 1997). In this derivation, virtual (or added) mass (second addend in bracketed expression) is a component of P^*_{acc}, whereas in our analysis based on instantaneous data it is included in P^*_{Aero}. To allow a direct comparison, we have therefore calculated separate power estimates, $P^*_{\text{acc,wing}}$ and $P^*_{\text{acc,virt}}$, for the contribution of wing and added mass, respectively (Table 1).

Results
Kinematics and aerodynamics of hovering flight

A selected example representing almost perfect hovering

Table 1. *Flight parameters and power estimates*

Fly number	n (Hz)	Φ (deg.)	$\overline{|d\hat{\phi}/df|^3}$	$\overline{(d\hat{\phi}/df)^2}$	$(d\hat{\phi}/df)^2_{max}$	Fly mass[a] (mg)	Fly mass[b] (mg)	Re	k	$\overline{C_L}$	$\overline{C_{D,pro}}$	$P^*_{Mech,low}$ (W kg⁻¹)	$P^*_{Mech,high}$ (W kg⁻¹)	$\overline{|P^*_{Acc}|}$ (W kg⁻¹)	$\overline{P^*_{Aero}}$ (W kg⁻¹)	$\overline{C_{D,pro,Re}}$	P^*_{ind}	P^*_{pro}	$P^*_{pro,Re}$	$P^*_{acc,wing}$	$P^*_{acc,virt}$	P^*_{acc}
Free																						
1	212	147	106	19.6	50.2	1.20	0.96	167	1.35	1.30	1.57	124	146	87	124	0.54	17	124	43	88	55	143
2	211	139	108	19.9	49.3	1.11	0.90	143	1.44	1.71	1.66	97	114	61	98	0.59	19	91	32	63	39	102
3	225	143	98	18.9	45.2	0.61	0.87	150	1.39	1.01	1.36	81	97	64	82	0.57	15	82	34	69	43	111
4	211	142	105	19.6	45.3	1.06	0.97	162	1.37	1.35	1.34	97	116	78	97	0.55	17	92	38	74	46	120
5	227	151	104	19.5	49.0	1.22	0.92	172	1.31	1.29	1.48	130	154	89	130	0.53	17	131	47	97	61	158
6	221	120	99	19.1	44.5	0.57	0.87	123	1.59	1.49	1.33	50	65	47	50	0.63	18	45	21	44	28	72
Mean	**218**	**140**	**103**	**19.4**	**47.2**	**0.96**	**0.91**	**153**	**1.41**	**1.36**	**1.46**	**97**	**115**	**71**	**97**	**0.57**	**17**	**94**	**36**	**72**	**45**	**118**
S.D.	7	10	4	0.3	2.3	0.27	0.04	17	0.09	0.21	0.13	27	30	15	27	0.03	1	28	8	17	11	28
Tethered																						
1	189	135	118	20.2	67.6	0.63	0.95	135	1.52	1.48	1.37	65	78	52	64	0.60	18	63	28	68	43	111
2	186	144	110	19.8	57.4	0.81	0.96	144	1.46	1.57	1.48	78	93	57	78	0.58	18	76	30	65	41	106
3	188	128	116	20.1	65.0	0.58	0.93	125	1.60	1.55	1.35	52	62	45	52	0.63	18	49	23	56	35	91
4	194	133	109	19.5	59.4	0.56	0.92	131	1.54	1.50	1.39	58	71	48	58	0.61	18	56	25	58	36	95
5	195	106	120	20.3	69.5	0.43	1.02	122	1.68	1.46	1.21	39	52	52	39	0.63	19	37	19	59	36	95
Mean	**191**	**129**	**114**	**20.0**	**63.8**	**0.60**	**0.96**	**131**	**1.56**	**1.51**	**1.36**	**58**	**71**	**51**	**58**	**0.61**	**18**	**56**	**25**	**61**	**38**	**100**
S.D.	4	14	5	0.3	5.2	0.14	0.04	9	0.08	0.05	0.10	15	15	4	14	0.02	0	14	4	5	3	9
Published[c]	**209**	**162**	**104.5**	**19.7**	**30.3**	**1.05**	–	–	**1.28**	–	–	–	–	–	–	**0.5–0.7**	**21.4**	**85.4**	**38.4**	**43.9**	**23.5**	**67.4**

[a]Estimated from lift; [b]estimated from regression on wing length; [c]Lehmann and Dickinson, 1997.
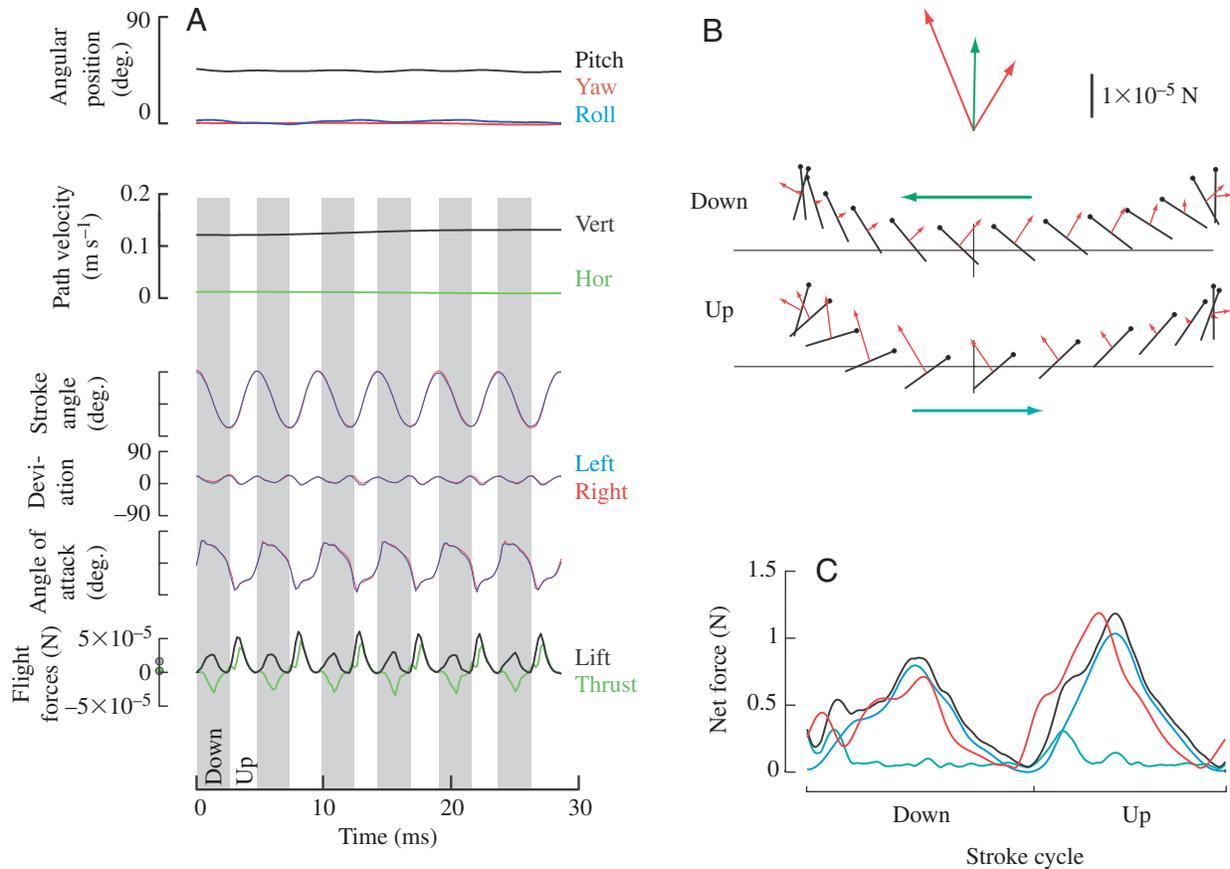
Fig. 2. Instantaneous wing kinematics and flight forces. (A) Body and wing kinematics measured during a slow vertical ascent. The body is pitched up by 45° (top, black trace) and the fly ascends at a constant velocity of about 0.12 m s^{-1}. The kinematics of the right (red) and left (blue) wing in the body frame (compare to Fig. 1C; the reference plane is inclined by 45° with respect to the long axis of the fly's body) are given below. Forward thrust and lift are shown at the bottom. (B) Average wing motion and instantaneous aerodynamic forces (red arrows) for the same data sample. Black lines indicate the position of the wing chord at 25 temporally equidistant points during the stroke cycle, with dots marking the leading edge. Green arrows show the direction of wing motion. The axes indicate a vertical range of stroke position between –90° to 90° horizontally and –10° to 10° vertically. The inset shows the mean downstroke and upstroke forces (red arrows), together with the average over the entire stroke (green arrow). (C) Quasi-steady analysis. The total aerodynamic force measured using the robotic wing (red trace) is compared with the flight force predicted by the model (black trace), which is composed of a translational (blue) and a rotational component (green). Calculations were performed using the model and code provided by W. B. Dickson (also see Dickson and Dickinson, 2004).

conditions (Fig. 2), permits the most straightforward test of the applied methods (a preliminary analysis of the sequence in the context of body saccades has appeared previously in Fry et al., 2003). We will show later that the wing kinematics and flight forces vary little among flight sequences, even in the case of non-zero advance ratios. During a period of 29 ms, or 6 wing strokes, the fly ascends slowly upward at a constant velocity of 0.13 m s^{-1} and a body pitch of 45° (Fig. 2A), in the absence of detectable body acceleration. Wing position (for definitions see Fig. 1C) follows a complicated, but highly regular, time course, suggesting a precise control of wing motion (also see Fig. 4A). Stroke deviation is substantial; the wing tip follows a roughly sinusoidal motion at twice the stroke frequency with a peak-to-peak amplitude of over 25°. Stroke position approaches a maximum of 90°, indicating that the wings are approximately parallel at the beginning of the downstroke. It was first suggested by Weis-Fogh (1975) that

small insects might augment forces *via* interaction between the wings as they pronate in close apposition, a mechanism known as the 'clap-and-fling'. In contrast, we never observed the wings making close contact during dorsal reversal in our experiments. Ennos (1989) reported findings for free flying *D. melanogaster* similar to ours, although he did observe one case of a fruit fly exhibiting the clap-and-fling.

A functional interpretation of the complex wing motion is possible by associating the measured wing trajectory with the resulting aerodynamic forces (Fig. 2B). The general pattern of the wing stroke is a 'U-shaped' wing trajectory. During the downstroke, the aerodynamic force increases to a maximum around mid-stroke and then decays toward the end of the downstroke (also see Fig. 2C). Wing reversal and supination are nearly synchronous, a phase relationship previously predicted to generate near optimal lift for a reciprocating pattern of wing motion ('symmetric case' in Sane and

Dickinson, 2001). The wing then begins to move backward and downward at an increasingly high velocity, causing a large force peak during the early phase of the upstroke. The average force generated by each half stroke (see inset of Fig. 2B) has a significant horizontal component, due to the high angle of attack. The horizontal force components cancel over the course of a stroke cycle, as expected for a hovering force balance, leaving only a vertical component of the total force vector.

Aerodynamic mechanisms

The simplest quasi-steady model, based on a single translation term, roughly follows the time course of the measured forces (Fig. 2C). Ignoring differences in the time course, the mean of the translational term is 89% of the mean of the measured force. However, this calculation is based on force coefficients measured in the absence of a periodic wake. Experiments indicate that translational forces drop roughly 10% due to induced flow within the wake (Birch and Dickinson, 2003), which would reduce the estimated contribution of translational forces to about 80%. Nevertheless, translational forces provide the main source of lift in hovering flight. The estimates of the translational component here are higher than prior estimates of 65%, based on phase-reconstructed tethered flight kinematics (Dickinson et al., 1999). This difference is most likely due to the increased aerodynamic angle of attack during the early part of each half stroke, a consequence of the 'U-shaped' trajectory of the wing, which is more prominent in the kinematics of free flying animals. This motion, though less extreme, is reminiscent of the upward force created by the vertical plunge during the
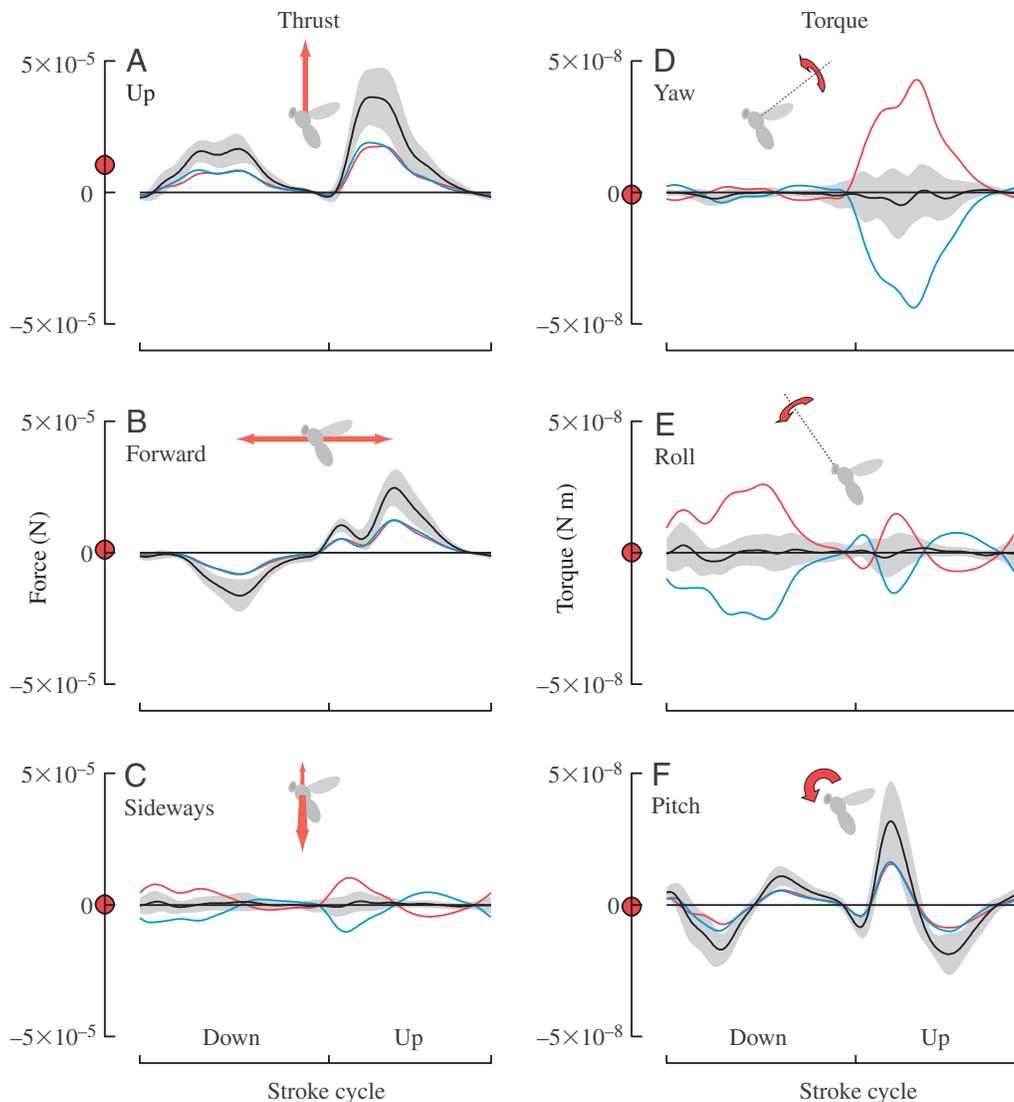

Fig. 3. Aerodynamic forces and torques during free hovering flight. (A–C) Translational forces over the course of the stroke cycle (abscissa). Red and blue traces show the forces generated by the right and left wing, respectively. The total force generated by the wings is shown in black, together with the s.d. (gray shaded area). The mean force over the duration of a stroke cycle is shown as a red dot on the ordinate. (A) Vertical force component, (B) forward thrust, (C) sideways thrust. (D–F) Torques. The same notation is used as in A–C. (D) Yaw torque, (E) roll torque, (F) pitch torque.

downstroke in dragonflies, which as recently discussed by Wang et al. (2003), is due primarily to wing drag. Analogously, the forces diminish toward zero as the stroke continues, because the aerodynamic angle of attack decays as the wing deviates upward.

However, when time-dependent effects may contribute to force production, comparisons of measured forces and theoretical models based on mean values may be misleading. For example, the time course of the measured forces exhibits a shoulder at the start of each half stroke that is not captured by the translational component. Addition of quasi-steady terms resulting from rotational forces (Sane and Dickinson, 2002; Walker, 2002) yields a prediction for the mean total force of 103%, but the measured forces still show a consistent advance relative to the multi-component quasi-steady model throughout the entire stroke (Fig. 2C). There are several possible explanations for this temporal shift. First, the quasi-steady model does not take into account any influence of the spatial and temporal dynamics of the wake, such as wake capture, the elevation in force immediately following stroke reversal (Dickinson et al., 1999), or the decrement in forces observed in long strokes due to the periodicity of downwash (Birch and Dickinson, 2001, 2003). Such effects would be consistent with the observed phase advance of measured forces relative to the quasi-steady model. Second, the quasi-steady model does not take into account the added mass force, which would be expected to increase total force at the start of the stroke, and decrease it at the end of the stroke (Birch and Dickinson, 2003). Although it is possible to derive a quasi-steady term for added mass force (Sane and Dickinson, 2002), these models do not accurately predict its time course when accelerations are large. This failure is due to a well-characterized hysteresis in added mass force, in which the force lags behind wing acceleration (Sarpkaya and Isaacson, 1981). Without more detailed information on the flow structure it is difficult to exclude the importance of wake effects or added mass in contributing to the unsteady component of the forces generated by the flapping wing.

Time history forces and moments

The most obvious requirement of hovering flight is the generation of a mean vertical force that precisely offsets the fly's own body weight. As shown in Fig. 3A, each wing provides a vertical force peak during the middle of each half stroke, with a considerably higher contribution from the upstroke. The relatively small variance among all six flight sequences is confirmation that the differences in wing motion for hovering and low advance ratio flight are quite small (note s.D. envelopes in Fig. 3). Because lift and drag are closely coupled, the wing creates large thrusts during each half stroke (Fig. 3B), but they sum nearly to zero over the course of a complete stroke cycle. Unlike forward thrust and lift, sideways thrust (sideslip) cancels instantly due to the bilateral symmetry of the wing motion (Fig. 3C). Similarly, because each wing contributes to yaw and roll torque with an opposite sense of direction, these moments sum to zero at each point in the stroke
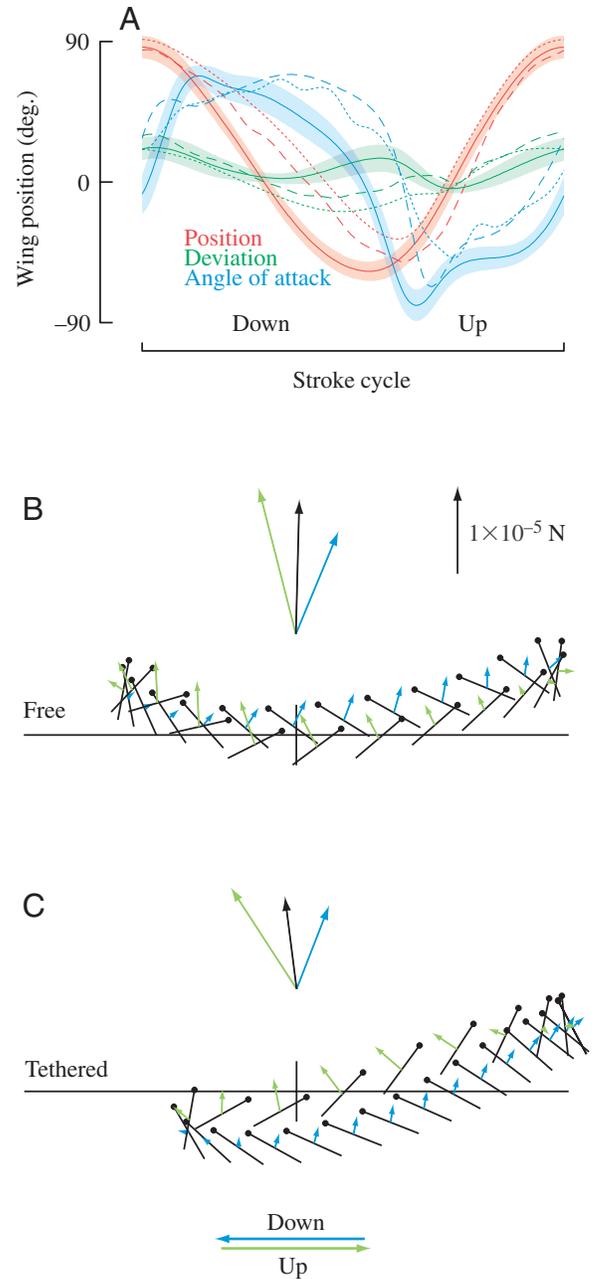

Fig. 4. Comparison between free and tethered flight. (A) Wing kinematics. Red, green and blue traces show the time course of stroke position, stroke deviation and angle of attack, respectively, over the course of a stroke cycle. Solid and broken lines show data from free and tethered flight, respectively. For comparison, data from a previous study using phase-reconstruction of separate stroboscopic images (Zanker, 1990a) are shown as dotted lines. Small differences of the coordinate systems used to measure wing position in this study may account for the discrepancy between the tethered flight measurements. (B) Wing motion and aerodynamic forces during free flight. For clarity, (mean) downstroke and upstroke forces are shown in blue and green, respectively. For details refer to the legend of Fig. 2B. (C) Same analysis as in B, except that data from tethered flies were used.

cycle, provided the motion of the two wings is bilaterally symmetric (Fig. 3D,E). Comparing the average peak

magnitude of yaw torque generated by one wing (48±14 nN m) indicates the precision with which flies must maintain symmetric wing motion. A net average yaw torque of less than 2 nN m is sufficient to initiate a body saccade, during which the angular velocity of the body can exceed 2000° s^{-1} (Fry et al., 2003). Thus, even a small bilateral change in wing motion would cause the animal to rotate.

The sign and magnitude of pitch torque is the same for both wings, resulting in a strongly fluctuating time course (Fig. 3F). As with forward thrust, pitch torque averages to zero over a complete cycle. These results also confirm that our methods provide reliable measurements of forces and torques.

Effects of tethering

Although tethered flight has previously been used as a proxy for free hovering flight, the effects of tethering have not been examined in careful detail. Our data reveal four consistent differences between the free and tethered conditions. (1) The stroke duty cycle is shifted such that downstroke takes up 60.4% of the cycle in tethered flight, as opposed to 53.8% in free flight (Fig. 4A). (2) The time course of stroke deviation is distorted in tethered flight. The wing continues to deviate downward to a minimum just prior to the ventral reversal, rather than moving upwards to create the 'U-shaped' trajectory characteristic of the free-flight pattern. (3) Compared to free flight (Fig. 4B), the total stroke amplitude is lower in tethered flight due to a reduction in the ventral (forward) extent of the stroke (Fig. 4C). (4) The stroke plane is tilted forward by about 12° with respect to the body axis under tethered conditions (Fig. 4C). These differences, though subtle, are large compared to the changes in kinematics responsible for free-flight maneuvers. For example, during body saccades the maximum difference in stroke angle between the wings is only 10° (fig. 3F in Fry et al., 2003). Although the time course of the morphological angle of attack is quite similar under free and tethered conditions, the difference in stroke deviation means
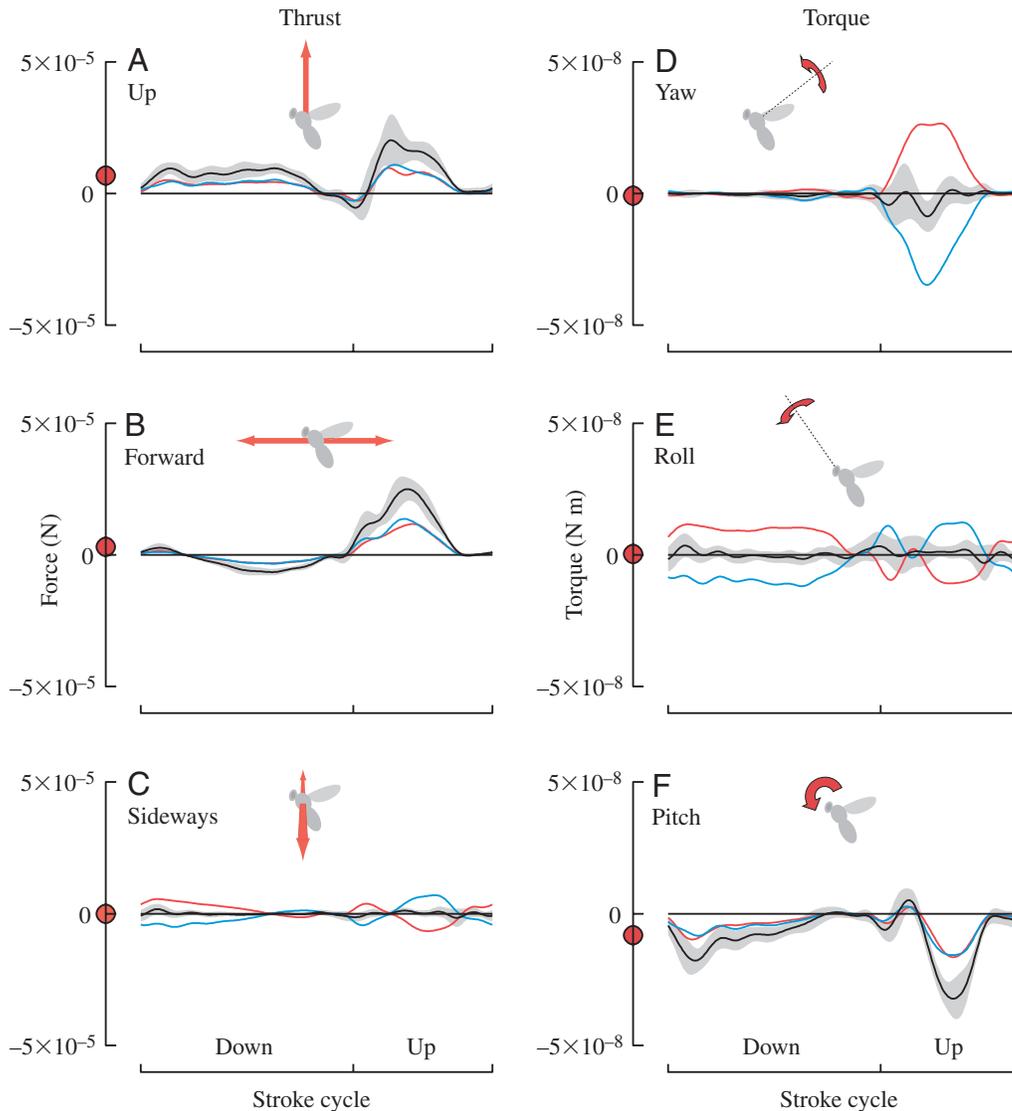

Fig. 5. Aerodynamic forces and torques during tethered flight. Refer to legend of Fig. 3 for details.

that that the aerodynamic angles of attack will vary throughout the stroke. The consistency of the tethered flight kinematics is indicated by the remarkably close match of our kinematics with those reported by Zanker (1990a, replotted as dotted lines in Fig. 4A), who reconstructed the wing motion by varying the phase of wingbeat-triggered stroboscopic images. The clap-and-fling is absent in our tethered kinematics, although it has been observed previous studies (Götz, 1987), an observation for which we have no immediate explanation.

To explore the effects of tethering on the force and torque output of the fly, we repeated the analysis of forces and torques using data acquired from tethered flying flies. Because the absolute body pitch angle is undefined for a tethered fly, we processed the tethered flight data for a hypothetical body pitch of 45° with respect to the horizontal, a value that corresponds closely to the measured value in the example shown in Fig. 2. The time course of forces under tethered and free-flight conditions share certain general features (Figs 5A–C, 3A–C). For example, the peak vertical forces generated during the upstroke are greater than those generated during the downstroke in both cases. This confirms direct measurements of instantaneous forces in tethered flight using laser

interferometry (Dickinson and Götz, 1996). However, the tethering does have noticeable effects on the time course and magnitude of force production. Compared with the results obtained from free flight, the mean total force vector is reduced in magnitude to 7.5±1.6 mN (–29%) and tilted forward by 17°. The average vertical force (for body pitch normalized to 45°) generated by tethered flies was 6.9±1.5 mN, well below the range of expected body weights (free flight: 10.0±2.8 mN, Table 1). The most pronounced effect is found in forward thrust, which on average reaches 3.0 mN (±0.6 mN) in tethered flight, although this value is based on our assumption that the animals' body orientation is equivalent to the free-flight condition. A comparison of the measured torques (Figs 5D–F, 3D–F) reveals that yaw and roll are also affected, but to a lesser degree. In contrast, tethering causes a pronounced nose-down pitch throughout almost the entire stroke cycle. The average nose-down pitch torque is 8.2±1.4 nN m, comparable to the peak yaw torques exerted during free-flight maneuvers (see above). This non-zero mean pitch is due to the low forces and reduced stroke amplitude at the end of the downstroke, just prior to ventral reversal. The measured pitch torque under tethered conditions would cause the fly to pitch nose-down by approximately 20° after a single wing stroke (for body dynamics refer to Fry et al., 2003).
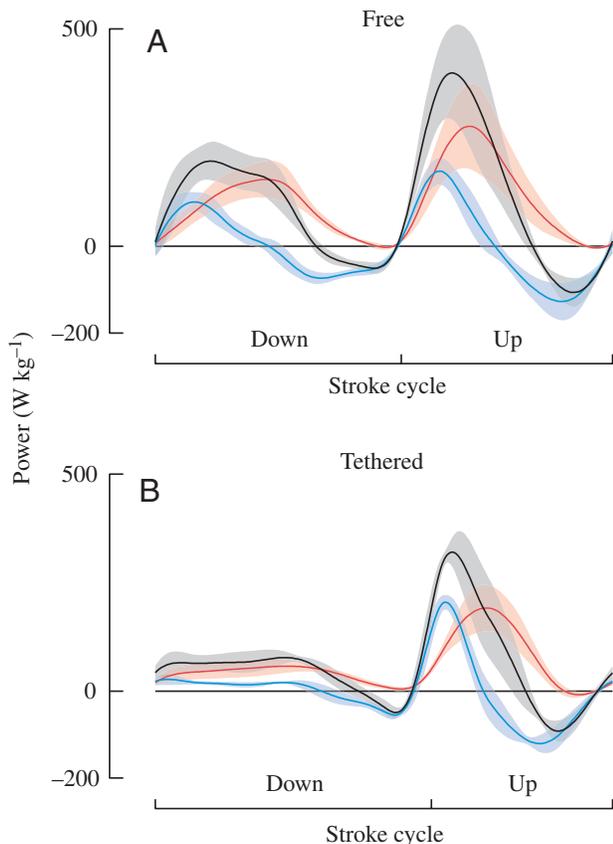
Power requirements

The measured instantaneous wing kinematics and aerodynamic forces permit a direct calculation of the instantaneous aerodynamic and inertial power over the course of a wing stroke (Eq. 3–6). The specific aerodynamic power, P^*_{Aero}, represents the power required to overcome air resistance, normalized to the mass of flight muscle (Eq. 3 and 6). P^*_{Aero} reaches a maximum near the middle of each half stroke, when wing velocity and aerodynamic force are maximal (Fig. 6A). The average aerodynamic power amounts to 97 W kg^{-1} (Table 1).

Specific inertial power, P^*_{Acc}, represents the power expended to accelerate the mass of the wing (Eq. 4 and 6). It is slightly lower in magnitude compared to aerodynamic power and follows a very different time course. Within each half stroke, P^*_{Aero} first increases as the wing accelerates, and then reverses sign as the wing decelerates. The average inertial power required to accelerate the wing (assuming that wing deceleration accrues no cost and there is not elastic storage) amounts to 71 W kg^{-1}.

The total mechanical power, P^*_{Mech}, is the instantaneous mechanical power required to move the wings, calculated from the sum of P^*_{Aero} and P^*_{Acc}. Around the middle of the downstroke, P^*_{Acc} becomes negative, due to the sign reversal of the inertial forces acting on the wing. P^*_{Mech} consequently decreases toward the end of the downstroke and becomes negative for a short period as the decelerating wings yield more power than is required to overcome aerodynamic forces. A similar pattern repeats during the upstroke.

The actual power that the flight muscles must generate, P^*_{Musc}, is not necessarily equivalent to P^*_{Mech}, because

Fig. 6. Instantaneous specific flight power. (A) Flight power during free flight. Traces show total mechanical power, P^*_{Mech} (black) and its aerodynamic (P^*_{Aero}, red) and inertial (P^*_{acc}, blue) components. Shaded areas show standard deviation. (B) Flight power during tethered flight.

negative mechanical power could be stored in elastic elements within the flight motor and recovered at the start of the next stroke (Dickinson and Lighton, 1995). The possible range of muscle power may be estimated by considering the consequences of 0% and 100% storage, with the added assumption that dissipated excess negative work does not accrue a net cost (also see Materials and methods). With no elastic storage, $P^*_{Musc}=P^*_{Mech,high}=115$ W kg^{-1}; with 100% elastic storage, $P^*_{Musc}=P^*_{Mech,low}=97$ W kg^{-1} (Table 1). In the case of perfect elastic storage there is no cost to wing acceleration and P^*_{Musc} consequently is equal to $\overline{P^*_{Aero}}$ (differences in the values for $P^*_{Mech,low}$ and $\overline{P^*_{Aero}}$ presented in Table 1 are due to rounding errors). Thus, the largest possible effect of elastic storage would amount to a reduction of only 19%, slightly higher than prior calculations for *D. hydei* (Dickinson and Lighton, 1995). In summary, provided there is no cost to negative work, the contribution of inertial cost is relatively small and may be further attenuated due to elastic storage. This suggests that – for *Drosophila* at least – estimates of flight costs based solely on aerodynamic power provide a reasonable estimate (within about 20%) of true energetic requirements.

Comparison with model-based estimates of muscle power

We calculated flight costs (Eq. 3–5) based on Ellington's time-averaged models (Ellington, 1984e) , for comparison with our new power estimates based directly on instantaneous kinematics and forces. Ellington's equations use a series on non-dimensional kinematic parameters that we were able to accurately calculate based on our instantaneous measurements. New and prior values for these input parameters are given in Table 1. The models predict two components of aerodynamic power: induced power (P^*_{ind}), the cost associated with accelerating a stream of air downwards to generate lift (Eq. 10), and profile power (P^*_{pro}), the cost associated with the drag acting on the wings (Eq. 12). The time-averaged estimate for inertial power (P^*_{acc}) combines the cost of accelerating both the wing mass and added mass.

Using our new values for mean stroke amplitude, Φ, mean lift, $\overline{F}_L$, and k, a wake periodicity correction factor, we calculated a P^*_{ind} value of 17.2 W kg^{-1} for our free-flight experiments and 18.0 W kg^{-1} for our tethered flight experiments. Both these values are just slightly lower than prior estimates based on tethered flight under conditions (21.4 W kg^{-1}), in which moving visual patterns were used to make the flies generate a lift force equal to body weight (Lehmann and Dickinson, 1997).

Profile power, P^*_{pro}, is linearly dependent on the mean profile drag coefficient $\overline{C_{D,pro}}$, which is difficult to predict without precise knowledge of wing kinematics and forces. For purposes of comparison, we estimated $\overline{C_{D,pro}}$ in two ways. First, a simple estimate based on the Reynolds number (Re) was obtained by applying Ellington's 7/sqrt(Re) approximation, which yields a value of 0.57 for our free-flight data (tethered: 0.61), similar to values used in previous studies (0.5–0.7, Dickinson and Lighton, 1995; Lehmann and Dickinson, 1997).

This simple approximation for $\overline{C_{D,pro}}$ yields a $P^*_{pro,Re}$ value of 36 W kg^{-1} for our free-flight experiments (tethered: 25 W kg^{-1}), similar to the previous estimate from tethered flies (38.4 W kg^{-1}; Lehmann and Dickinson, 1997; Table 1). The second, more accurate, value for $\overline{C_{D,pro}}$ was obtained from measured profile drag and wing kinematics (Eq. 14), and yields a much higher value of 1.46 (tethered: 1.36), consistent with recent measurements of wing drag coefficients at the angles of attack used throughout the stroke (Dickinson et al., 1999; Sun and Tang, 2002). Using these higher, more accurate numbers for the mean drag coefficient results in a substantially higher P^*_{pro} value of 94 W kg^{-1} (tethered: 56 W kg^{-1}).

A comparison of the muscle power predicted by the time-averaged models and those based on instantaneous power must be made with close scrutiny of the underlying assumptions. Muscle power must be at least as high as the predicted aerodynamic power, if inertial components are assumed negligible. The total aerodynamic cost predicted by Ellington's model using the improved estimates for P^*_{pro}, is 111 W kg^{-1} for free flight and 74 W kg^{-1} for tethered flight (calculated from the sum of P^*_{ind} and P^*_{pro}). This value is slightly higher than our estimates of P^*_{Aero} based on instantaneous forces and kinematics, although the power associated with the acceleration of added mass, $P^*_{acc,virt}$ (Eq. 15), is not included, which would tend to increase the magnitude of the discrepancy. As a component of inertial power in Ellington's models, added mass has been previously assumed to function similarly to the wing mass, as such accruing no extra cost given even moderate elastic storage. Assuming that added mass does contribute to flight cost, even when the cost of wing mass inertia is nullified by elastic storage, we calculate flight power from the sum of P^*_{ind}, P^*_{pro} and $\frac{1}{2}P^*_{acc,virt}$, yielding 134 W kg^{-1}. The term of $\frac{1}{2}$ in this rough calculation follows from Ellington's original definitions and assumes that negative work accrues zero cost. This value is substantially higher than our estimate based on instantaneous forces, in which added mass contributions are also included in aerodynamic power (97 W kg^{-1}). In summary, the results suggest that time-averaged models are likely to overestimate the power requirements of hovering flight.

Discussion

To explore the aerodynamic performance and control of hovering flight, we chose an approach consisting of two key components. First, our analyses were based on the time-resolved 3D kinematics of free flying animals, a critical requirement for an unambiguous analysis of hovering flight performance (Weis-Fogh and Jensen, 1956; Ellington, 1984a). Second, by replaying the kinematics through a dynamically scaled robot, we were able to more directly estimate the instantaneous forces, torques and power for a detailed analysis of hovering aerodynamics. The time-resolved aerodynamic forces were compared to a multi-component quasi-steady model, which predicted the time course and magnitude of measured forces with reasonable accuracy (Fig. 2C). However,

we did observe a consistent phase lead of measured force relative to the model that may reflect the time-dependent influence of the wake on force production (Birch and Dickinson, 2003), as well as a hysteresis in the development of added mass forces (Sarpkaya and Isaacson, 1981).

Because we independently measured the kinematics of both wings, we were able to determine the time history of forces and moments controlling all six degrees of freedom (Fig. 3). Our results indicate that the need to balance thrust, lift and pitch imposes severe constraints on the spatio-temporal pattern of wing motion. In particular, the speed and precision with which flies must control torque suggests that rapid sensory-motor feedback circuits are required to regulate wing motion. This control takes place within a complex set of constraints imposed by the requirements of balancing six degrees of motion within each stroke, the physiology of the flight apparatus, and the dynamics of the oscillatory wing motion. A detailed comparison with data from freely flying flies shows that the wing motion of tethered flies is distorted in a stereotyped manner (Fig. 4), resulting in a large tonic pitch-down moment (Fig. 5). Finally, we provide a direct estimation of muscle power based on instantaneous mechanical power, which yields a value almost twice that of prior estimates based on time-averaged models. Much of this discrepancy can be explained by a 2.5-fold underestimate of the actual mean drag coefficient in prior models. However, if implemented with more accurate input parameters, including more realistic values for the mean drag coefficient, the time-averaged models tend to overestimate flight cost, which brings into question their reliability.

Requirements for flight control

To hover stably and efficiently, a fly must generate sufficiently large and precisely balanced flight forces, while minimizing energetic costs – a substantial challenge given that all forces and moments in hovering flight are produced by the two rapidly reciprocating wings. Although our analysis does not address flight control experimentally, it does reveal the requirement for highly precise and fast control of wing kinematics on a stroke-by-stroke basis. Because a flapping wing creates high force transients during the stroke cycle, even the slightest variation in wing motion can rapidly alter the fly's orientation, implying that the same rapid sensory-motor control systems are being used during hovering flight as for saccadic turning maneuvers (Fry et al., 2003). For example, a net average torque of less than 2 nN m, or 4% of the peak yaw torque produced by a single wing during hovering flight, is sufficient to initiate a saccade, during which the angular velocity of the body can reach 2000 deg. s^{-1} within a few wing beats (Fry et al., 2003). The control of roll is even more sensitive because the moment of inertia around the roll axis is considerably lower compared to that of pitch and yaw, due to the elongated shape of the body.

In contrast to body motion outside the mid-sagittal plane (yaw, roll and sideways thrust), body motion within the mid-sagittal plane (pitch, upward and forward thrust) requires symmetric changes in stroke pattern that act over the course of a stroke cycle, imposing severe constraints on the spatio-temporal pattern of force production. The high sensitivity of net pitch torque to changes in the stroke pattern is illustrated in tethered flies, where a moderate distortion of the spatio-temporal pattern of wing motion leads to a strong nose-down pitch torque (Fig. 5F).

The neural and morphological mechanisms that allow flies to exert the observed precise kinematic control remain poorly understood. The complex morphology of the wing hinge, together with the resonant dynamics of the oscillating wing motion, may provide mechanical constraints that permit a limited number of steering muscles to generate gradual and precise modifications of stroke patterns for flight control and maneuvering (Tu and Dickinson, 1996; Balint and Dickinson, 2001). There are several lines of indirect evidence for the importance of such mechanical constraints in flies. As shown in this study, the pattern of wing motion is highly stereotyped and frequency-invariant (Fig. 4), at least during slow flight. The comparison between free and tethered hovering data (Figs 3, 5) demonstrates how various kinematic parameters change in concert, including stroke amplitude, mean stroke position, stroke phase, stroke plane angle and, to a lesser degree, angle of attack. Further, the wing kinematics observed in free and tethered flight during turning maneuvers indicate that flight control is mediated by highly correlated changes in stroke amplitude, deviation, angle of attack and frequency (tethered flying *Calliphora*: Balint and Dickinson, 2004; free flying *Drosophila*: Fry et al., 2003). From the perspective of flight control, the intrinsic coupling of flight motor dynamics and mechanics represents the physical backdrop upon which the animal's flight control system evolved the appropriate control inputs. Determining how the nervous system has coevolved with the musculo-skeletal system to produce such impressive performance despite these constraints represents a formidable challenge for future research.

Effects of tethering

Tethered flight preparations have been used extensively to study the neurobiology, physiology and behavior of flight in *Drosophila* and many other insects and is likely to remain an important experimental paradigm. To more accurately assess the potential behavioral artifacts introduced by tethering, we performed experiments in free flying flies and compared the results with those obtained from tethered flies under otherwise similar experimental conditions. Tethered flies generate a pattern of wing motion that is clearly different from those obtained during free flight (Fig. 4). The fact that our measurements of tethered flies are consistent both between flies and with Zanker's earlier measurements (Zanker, 1990a) suggests that the distortions introduced by tethering are stereotyped and result from a consistent mechanical or sensory effect. Such distortions might result from a tonically activated equilibrium reflex response, elicited by unnatural reafferent sensory feedback under tethered conditions. The work of David (1978) indicates that fruit flies regulate flight speed in part through changes in body pitch, such that the animal pitches

nose-down to increase flight speed, much like a helicopter. Further, in free flight *Drosophila* exhibit a preferred ground speed of about 10 cm s^{-1} (David, 1982). Thus, one possibility is that stationary tethering might alter the animal's flight velocity control system, resulting in a continuous attempt to accelerate forward. An alternative, but not mutually exclusive, line of reasoning is that tethering introduces a direct mechanical artifact that distorts the action of the indirect flight muscles and the wing hinge. At this point we cannot distinguish between these two hypotheses. However, recent measurements of wing kinematics in free flying individuals at higher advance ratios are similar to those of tethered flies (R. Sayaman, unpublished observation). This supports the view that the artificial sensory conditions during tethered flight elicit an inappropriate, but not necessarily unnatural, stroke pattern. In spite of the significant changes in wing kinematics, tethered flies nevertheless show a similar pattern of translational forces and a meaningful optomotor response (e.g. Götz, 1968; Heisenberg and Wolf, 1993). The recent insights into free-flight dynamics (Fry et al., 2003) and those from the present report may serve a better interpretation of tethered flight responses with respect to their function in free flight under real-world conditions.

Power

The utility of capturing the instantaneous kinematics and forces of freely hovering animals is particularly evident in the estimation of mean muscle power. Only under free-flight conditions is it guaranteed that a fly generates the power required to hover and that its aerodynamic force output truly reflects hovering conditions. Unlike time-averaged estimates of flight power, the measured instantaneous mechanical power allows a more direct calculation of mean muscle power and thus an improved estimate of muscle efficiency and the effects of elastic storage. Our value for *Drosophila melanogaster* (97 W kg^{-1}) is almost exactly the same as a recent estimate (95.7 W kg^{-1}) based on a computational fluid dynamics (CFD) model of flight forces and power costs in a closely related species, *D. virilis* (Sun and Tang, 2002). These experiments confirm previous studies (Dickinson and Lighton, 1995) that even a moderate amount of elastic storage would be sufficient to eliminate the cost of inertial power, provided that negative work accrues no energetic cost.

These direct power estimates also allow us to test the accuracy of time-averaged models used to predict flight power. The results of this comparison indicate that prior estimates are likely to have underestimated the cost of hovering flight by a factor of nearly two (Lehmann and Dickinson, 1997). The primary reason for this underestimate is that prior work employed Ellington's 7/sqrt(*Re*) estimate for the mean drag coefficient, which our direct force measurements indicate is approximately 2.5 times too low, confirming recent findings (Dickinson and Götz, 1996; Dickinson et al., 1999; Ellington, 1999; Usherwood and Ellington, 2002). Given that *Drosophila* fly at a relatively low Reynolds number, the error for larger hovering insects is likely to be even greater. However, in the case of *Drosophila* at least, the assessment of time-averaged estimates is more complicated. In addition to providing better estimates of the mean drag coefficient, our 3D free-flight data provide more accurate values for the kinematic input parameters to the time-averaged models. When these values are used, the models slightly overestimate aerodynamic power compared to the values based on instantaneous forces (111 W kg^{-1} *vs* 97 W kg^{-1}; Table 1). This discrepancy is greater, however, if the added mass term is combined with the time-averaged estimate, which results in a value of 134 W kg^{-1}. The comparison also reveals the difficulty related to the reliable measurement or estimation of the input parameters used in Ellington's models. Estimating muscle power based on high-speed videography is likewise based on a number of basic assumptions including, for example, the positions of the center of pressure and mass on the wing. Furthermore, our calculation of specific muscle power critically depends on knowledge of the body mass, which we inferred indirectly from a regression on wing length. In spite of these limitations, the parameters used in our calculations are well founded by independent measurements and subject to a limited margin of error. In particular, the calculations of instantaneous power do not require higher order terms that tend to amplify errors. Although the time-averaged models have provided a remarkably useful tool for insect flight research prior to recent advances in high speed imaging and data processing, we suggest that the more direct measurement of flight power or numerical simulation may present a more practical solution for future research.

List of symbols

a	wing area
$\bar{c}$	mean chord length
$\overline{C_{D,pro}}$	mean profile drag coefficient
$\overline{C_L}$	mean lift coefficient
$\overline{\|d\hat{\phi}/d\hat{t}\|^3}$	mean cube of the absolute value of non-dimensional angular velocity
$\overline{(d\hat{\phi}/d\hat{t})^2}$	mean square of the non-dimensional wing velocity
$(d\hat{\phi}/d\hat{t})_{max}^2$	square of the maximum non-dimensional wing velocity
F_{fly}	magnitude of aerodynamic forces acting on an actual fly
F_{Robot}	magnitude of aerodynamic forces acting on the robotic model
$\overline{F_D}$	mean drag
$\overline{F_L}$	mean lift
$\mathbf{F_{Acc}}$	inertial force
$\mathbf{F_{Aero}}$	aerodynamic force
$\boldsymbol{g}$	gravitational constant
$\hat{h}$	non-dimensional wing thickness
k	Rankine-Froude correction factor
l	wing length
M_b	body mass
M_M	mass of flight muscle

M_{Wing}	wing mass
n	stroke frequency
P_{Aero}	instantaneous aerodynamic power
P_{Acc}	instantaneous inertial power
P_{Mech}	instantaneous mechanical power
P_{Musc}	mean muscle power
$P_{\mathrm{acc,\,win}g}$	inertial power due to wing mass
$P_{\mathrm{acc,\,virt}}$	inertial power due to added mass
P_{ind}	induced power
P_{pro}	profile power
P^{*}	specific power, normalized with respect to $_{\mathrm{MM}}$, e.g. P^{*}_{acc} specific inertial power, etc.
$\mathbf{r}$	moment arm of flight force
$\hat{r}_2^2(S)$	non-dimensional second moment of wing area
$\hat{r}_2^2(m)$	non-dimensional second moment of wing mass
$\hat{r}_2^2(v)$	non-dimensional second moment of wing virtual mass
$\hat{r}_3^3(S)$	non-dimensional third moment of wing area
R	wing length
Re	Reynolds number
S	wing area
$\hat{t}$	non-dimensional duration of the wing stroke
$\mathbf{T}_{\mathrm{Aero}}$	aerodynamic torque
$\mathbf{U}_{\mathrm{M}}$	velocity of wing at center of mass
$\mathbf{U}_{\mathrm{P}}$	velocity of wing at center of pressure
$\hat{v}$	non-dimensional virtual (added) mass
Φ	stroke amplitude
ρ	fluid density
ω_0	induced velocity

References

Balint, C. N. and Dickinson, M. H. (2001). The correlation between wing kinematics and steering muscle activity in the blowfly *Calliphora vicina*. *J. Exp. Biol.* **204**, 4213-4226.

Balint, C. N. and Dickinson, M. H. (2004). Neuromuscular control of aerodynamic forces and moments in the blowfly, *Calliphora vicina*. *J. Exp. Biol.* **207**, 3813-3838.

Birch, J. M. and Dickinson, M. H. (2001). Spanwise flow and the attachment of the leading-edge vortex on insect wings. *Nature* **412**, 729-733.

Birch, J. M. and Dickinson, M. H. (2003). The influence of wing–wake interactions on the production of aerodynamic forces in flapping flight. *J. Exp. Biol.* **206**, 2257-2272.

Birch, J. M., Dickson, W. B. and Dickinson, M. H. (2004). Force production and flow structure of the leading edge vortex on flapping wings at high and low Reynolds numbers. *J. Exp. Biol.* **207**, 1063-1072.

Buckholz, R. H. (1981). Measurements of unsteady periodic forces generated by the blowfly flying in a wind tunnel. *J. Exp. Biol.* **90**, 163-173.

Cloupeau, M., Devillers, J. F. and Devezeaux, D. (1979). Direct measurements of instantaneous lift in desert locust; comparison with Jensen's experiments on detached wings. *J. Exp. Biol.* **80**, 1-15.

Craven, P. and Wahba, G. (1979). Smoothing noisy data with spline functions. *Numerische Mathematik* **31**, 377-403.

David, C. T. (1978). The relationship between body angle and flight speed in free-flying *Drosophila*. *Physiol. Entomol.* **3**, 191-195.

David, C. T. (1982). Compensation for height in the control of groundspeed by *Drosophila* in a new, 'Barber's Pole' wind tunnel. *J. Comp. Physiol.* **147A**, 485-493.

Dickinson, M. H. (1999). Haltere-mediated equilibrium reflexes of the fruit fly, *Drosophila melanogaster*. *Phi1. Trans. R. Soc. Lond. B* **354**, 903-916.

Dickinson, M. H. and Götz, K. G. (1996). The wake dynamics and flight forces of the fruit fly *Drosophila melanogaster*. *J. Exp. Biol.* **199**, 2085-2104.

Dickinson, M. H., Lehmann, F. O. and Sane, S. P. (1999). Wing rotation and the aerodynamic basis of insect flight. *Science* **284**, 1954-1960.

Dickinson, M. H. and Lighton, J. R. B. (1995). Muscle efficiency and elastic storage in the flight motor of *Drosophila*. *Science* **268**, 87-90.

Dickson, W. B. and Dickinson, M. H. (2004). The effect of advance ratio on the aerodynamics of revolving wings. *J. Exp. Biol.* **207**, 4269-4281.

Dudley, R. (2000). *The Biomechanics of Insect Flight: Form, Function, Evolution*. Princeton: Princeton University Press.

Ellington, C. P. (1984a). The aerodynamics of hovering insect flight. *Phil. Trans. R. Soc. Lond. B* **305**, 1-181.

Ellington, C. P. (1984b). The aerodynamics of hovering insect flight. II. Morphological parameters. *Phil. Trans. R. Soc. Lond. B* **305**, 17-40.

Ellington, C. P. (1984c). The aerodynamics of hovering insect flight. III. Kinematics. *Phil. Trans. R. Soc. Lond. B* **305**, 41-78.

Ellington, C. P. (1984d). The aerodynamics of hovering insect flight. V. A vortex theory. *Phil. Trans. R. Soc. Lond. B* **305**, 115-144.

Ellington, C. P. (1984e). The aerodynamics of hovering insect flight. VI. Lift and power requirements. *Phil. Trans. R. Soc. Lond. B* **305**, 145-181.

Ellington, C. P. (1999). The novel aerodynamics of insect flight: applications to micro-air vehicles. *J. Exp. Biol.* **202**, 3439-3448.

Ennos, A. R. (1989). The kinematics and aerodynamics of the free flight of some diptera. *J. Exp. Biol.* **142**, 49-85.

Fry, S. N., Sayaman, R. and Dickinson, M. H. (2003). The aerodynamics of free-flight maneuvers in *Drosophila*. *Science* **300**, 495-498.

Frye, M. A., Tarsitano, M. and Dickinson, M. H. (2003). Odor localization requires visual feedback during free flight in *Drosophila melanogaster*. *J. Exp. Biol.* **206**, 843-855.

Götz, K. G. (1968). Flight control in *Drosophila* by visual perception of motion. *Kybernetik* **4**, 199-208.

Götz, K. G. (1987). Course-control, metabolism and wing interference during ultralong tethered flight in *Drosophila melanogaster*. *J. Exp. Biol.* **128**, 35-46.

Haslwanter, T. (1995). Mathematics of three-dimensional eye rotations. *Vision Res.* **35**, 1727-1739.

Heisenberg, M. and Wolf, R. (1993). The sensory-motor link in motion-dependent flight control of flies. *Rev. Oculomot. Res.* **5**, 265-283.

Lehmann, F. O. and Dickinson, M. H. (1997). The changes in power requirements and muscle efficiency during elevated force production in the fruit fly *Drosophila melanogaster*. *J. Exp. Biol.* **200**, 1133-1143.

Lehmann, F. O. and Dickinson, M. H. (1998). The control of wing kinematics and flight forces in fruit flies (*Drosophila* spp.). *J. Exp. Biol.* **201**, 385-401.

Nalbach, G. (1993). The halteres of the blowfly *Calliphora*: I. Kinematics and dynamics. *J. Comp. Physiol. A* **173**, 293-300.

Nalbach, G. and Hengstenberg, R. (1994). The halteres of the blowfly *Calliphora*: II. Three-dimensional organization of compensatory reactions to real and simulated rotations. *J. Comp. Physiol. A* **175**, 695-708.

Ramamurti, R. and Sandberg, W. (2002). A three-dimensional computational study of the aerodynamic mechanisms of insect flight. *J. Exp. Biol.* **205**, 1507-1518.

Sane, S. P. and Dickinson, M. H. (2001). The control of flight force by a flapping wing: lift and drag production. *J. Exp. Biol.* **204**, 2607-2626.

Sane, S. P. and Dickinson, M. H. (2002). The aerodynamic effects of wing rotation and a revised quasi-steady model of flapping flight. *J. Exp. Biol.* **205**, 1087-1096.

Sarpkaya, T. and Isaacson, M. (1981). *Mechanics of Wave Forces on Offshore Structures*. New York: Van Nostrand Reinhold.

Sherman, A. and Dickinson, M. H. (2003). A comparison of visual and haltere-mediated equilibrium reflexes in the fruit fly *Drosophila melanogaster*. *J. Exp. Biol.* **206**, 295-302.

Stark, W. S. and Johnson, M. (1980). Microspectrophotometry of *Drosophila* visual pigments: determinations of conversion efficiency in R1-6 receptors. *J. Comp. Physiol. A* **140**, 275-286.

Sun, M. and Lan, S. L. (2004). A computational study of the aerodynamic

forces and power requirements of dragonfly (*Aeschna juncea*) hovering. *J. Exp. Biol.* **207**, 1887-1901.

Sun, M. and Tang, J. (2002). Lift and power requirements of hovering flight in *Drosophila virilis*. *J. Exp. Biol.* **205**, 2413-2427.

Sun, M. and Wu, J. H. (2003). Aerodynamic force generation and power requirements in forward flight in a fruit fly with modeled wing motion. *J. Exp. Biol.* **206**, 3065-3083.

Taylor, G. K. (2001). Mechanics and aerodynamics of insect flight control. *Biol. Rev. Camb. Phil. Soc.* **76**, 449-471.

Tu, M. S. and Dickinson, M. H. (1996). The control of wing kinematics by two steering muscles of the blowfly (*Calliphora vicina*). *J. Comp. Physiol. A* **178**, 813-830.

Usherwood, J. R. and Ellington, C. P. (2002). The aerodynamics of revolving wings I. Model hawkmoth wings. *J. Exp. Biol.* **205**, 1547-1564.

Wakeling, J. E. and Ellington, C. P. (1997). Dragonfly flight. II. Velocities, accelerations and kinematics of flapping flight. *J. Exp. Biol.* **200**, 557-582.

Walker, J. A. (2002). Rotational lift: Something different or more of the same? *J. Exp. Biol.* **205**, 3783-3792.

Wang, H., Zeng, L., Liu, H. and Yin, C. (2003). Measuring wing kinematics, flight trajectory and body attitude during forward flight and turning maneuvers in dragonflies. *J. Exp. Biol.* **206**, 745-757.

Weis-Fogh, T. (1972). Energetics of hovering flight in hummingbirds and *Drosophila*. *J. Exp. Biol.* **56**, 79-104.

Weis-Fogh, T. (1973). Quick estimates of flight fitness in hovering animals, including novel mechanisms for lift production. *J. Exp. Biol.* **59**, 169-230.

Weis-Fogh, T. (1975). Unusual mechanisms for the generation of lift in flying animals. *Sci. Am.* **233**, 81-87.

Weis-Fogh, T. and Jensen, M. (1956). Biology and physics of locust flight. I. Basic principles in insect flight. A critical review. *Phil. Trans. R. Soc. Lond. B* **239**, 415-458.

Willmott, A. P. and Ellington, C. P. (1997). The mechanics of flight in the hawkmoth *Manduca sexta*. I. Kinematics of hovering and forward flight. *J. Exp. Biol.* **200**, 2705-2722.

Wu, J. H. and Sun, M. (2004). Unsteady aerodynamic forces of a flapping wing. *J. Exp. Biol.* **207**, 1137-1150.

Zanker, J. M. (1990a). The wing beat of *Drosophila melanogaster* I. Kinematics. *Phil. Trans. R. Soc. Lond. B* **327**, 1-18.

Zanker, J. M. (1990b). The wing beat of *Drosophila melanogaster* II. Dynamics. *Phil. Trans. R. Soc. Lond. B* **327**, 19-44.